Available online at www.sciencedirect.com
ScienceDirect
Geochimica et Cosmochimica Acta 71 (2007) 5267–5285
Geochimica et Cosmochimica Acta
www.elsevier.com/locate/gca

Dynamic crystallization of shock melts in Allan Hills 77005: Implications for melt pocket formation in Martian meteorites

Erin L. Walton *, Christopher D.K. Herd

Department of Earth and Atmospheric Sciences, University of Alberta, 1-26 Earth Sciences Building, Edmonton, AB., Canada T6G 2E3

Received 26 February 2007; accepted in revised form 5 September 2007; available online 20 September 2007

Abstract

A series of crystallization experiments have been performed on synthetic glasses matching the composition of a melt pocket found in Allan Hills (ALH) 77005 in order to evaluate the heterogeneous nucleation potential of the melt and the effect of oxygen fugacity on crystallization. The starting temperature of the experiments varied from superliquidus, liquidus and subliquidus temperatures. Each run was then cooled at rates of 10, 500 and 1000 °C/h at FMQ. The results of this study constrain the heating and cooling regime for a microporphyritic melt pocket. Within the melt pocket, strong thermal gradients existed at the onset of crystallization, giving rise to a heterogeneous distribution of nucleation sites resulting in gradational textures of olivine and chromite. Skeletal olivine in the melt pocket center crystallized from a melt containing few nuclei cooled at a fast rate. Nearer to the melt pocket margin elongate skeletal shapes progress to hopper and equant euhedral, reflecting an increase in nuclei in the melt at the initiation of crystallization and growth at low degrees of supercooling. Cooling from post-shock temperatures took place on the order of minutes.

An additional series of experiments were conducted for a melt temperature of 1510 °C and a cooling rate of 500 °C/h at the FMQ buffer, as well as 1 and 2 log units above and below FMQ. Variation in chromite stability in these experiments is reflected in crystal shapes and composition, and place constraints on the oxygen fugacity of crystallization of the melt pocket. We conclude that the oxygen fugacity of the melt pocket was set by the Fe^{3+}/Fe^{2+} ratio imparted by melting of the host rock, rather than external factors such as incorporation of CO_2-rich Martian atmosphere, or melting and injection of oxidized surface (e.g., regolith) material.

Comparison with previous crystallization experiments on melt pockets in Martian basalts indicate that the predominance of dendritic crystal shapes reflects the likelihood that those melt pockets with lower liquidus temperatures will be more completely melted, destroying most or all nuclei in the melt. In this case, crystal growth takes place at high degrees of supercooling, yielding dendritic shapes. It appears as though the melting process is just as important as cooling rate in determining the final texture of the melt pocket, as this process controls elimination or preservation of nuclei at the onset of cooling and crystallization.

1. INTRODUCTION

Melt pockets occur as irregular to subrounded enclaves of silicate glass and crystals, heterogeneously distributed throughout the groundmass of strongly shocked shergottite meteorites. Analysis of melt pocket separates and *in situ* laser probe work have shown that the melt pockets are the specific carrier of the largest amounts of Martian atmosphere in the meteorites, defined by the relative concentration and isotopic composition of noble gases, N_2 and CO_2 (Bogard and Johnson, 1983; Becker and Pepin, 1984; Wiens et al., 1984; Carr et al., 1985; Marti et al., 1995; Walton

* Corresponding author.
E-mail address: ewalton@ualberta.ca (E.L. Walton).

0016-7037/$ - see front matter © 2007 Elsevier Ltd. All rights reserved.
doi:10.1016/j.gca.2007.09.002

et al., 2007). Laboratory shock experiments have shown that ambient gases can be implanted into basalt by shock in relatively large amounts and at moderately low shock pressures without mass fractionation of heavy noble gases and nitrogen (Bogard et al., 1986; Wiens and Pepin, 1988). These experiments were also successful in producing shock-generated glasses. Shock in general is thus accepted as a reasonable process for forming melt pockets and trapping the gases within them.

The close match between gases extracted from melt pockets with that of the Martian atmosphere (Owen et al., 1977) remains the most concrete evidence supporting a Martian origin for Shergottite Nakhlite Chassignite (SNC) meteorites (hereafter referred to as Martian meteorites). As first noted by Bogard et al. (1986), atmospheric gases are preferentially trapped in the shock-generated melts; thus, the mode of formation of these melts becomes crucial to understanding the implantation mechanism. To date, there have been over 2000 journal articles and conference abstracts published on the topic of Martian meteorites (Meyer, 2007). The main motive for such studies is that observations of the meteorites can be generalized to become probable observations of Mars. Thus, the issue of melt pocket formation has relevance to the study of Martian meteorites in general. Despite early recognition of the importance of melt pocket studies, the origin of melt pockets remains a topic of debate (see following paragraph) and their crystallization conditions are not well constrained. This study reports on the results of dynamic crystallization experiments performed at 1 bar on the bulk composition of a shock-generated melt pocket in lherzolitic basaltic Martian meteorite Allan Hills (ALH) 77005. The goal is to produce experimentally, textures which resemble those observed in the natural sample in order to constrain the post-shock cooling history of melt pockets. The results of such crystallization experiments have bearing on the issue of trapped Martian atmospheric gases, because it is during the liquid stage of melt pocket evolution that the atmosphere becomes trapped in the melt pockets and during cooling that the melt pockets have the potential to lose gases.

Mechanism(s) for melt pocket formation can be divided into two scenarios, the first involving injection of extraneous molten material, possibly including Martian regolith, into cracks and fractures in the host rock, and the second, *in situ* localized melting by shock impedance contrasts. Shock impedance is the shock wave velocity multiplied by the relative density of a phase (i.e., specific gravity, G). For the latter mechanism, the most extreme case would represent collapse of pore space ($G \approx 0$) in the host rock ($G \approx 3$–5), producing the highest dissipation of energy (Heider and Kenkmann, 2003). Each scenario (injection versus *in situ*) is not without problems. For the injection mechanism, earlier studies concentrated on large cm-size melt pockets in Elephant Moraine (EET) 79001, the first meteorite found to contain Martian atmospheric gases (Bogard and Johnson, 1983). EET 79001 melt pockets (lithology C) exhibit sharp boundaries with the host rock, cited as evidence in support of injection. Subsequent surveys of melt pockets in the groundmass of other Martian meteorites show that such cm-size pockets appear to be anomalously large compared to the much smaller (in apparent diameter) mm- and μm-size melt pockets and veins that are more typically observed. In addition, gradational melt pocket/host rock interfaces, and that the bulk composition of some melt pockets reflects local mineral-scale melting, remain problems for the injection mechanism. Injected material would be expected to exhibit sharp boundaries with the host rock, as is observed in terrestrial impact structures. The injection scenario must also account for pockets and veins of such size (1–200 μm) to provide conduits for the injected molten material. However, it is difficult to envision melts traveling more than a few cm along such minute conduits in the host rock. Arguments against *in situ* formation remain that earlier studies (Wooden et al., 1982; Nyquist et al., 1986), report evidence that melt pockets in EET 79001 are heterogeneous in Sr isotopic ratios, beyond the range of mineral separates analyzed from the host rock (lithology A). This is supported by high-vacuum pyrolysis of EET 79001 host rock (lithology A) and melt pocket chips (Gooding and Muenow, 1986), which produced sulfur in different proportions of oxidized (SO_2) and reduced (H_2S, S_2) species, with the melt pocket possessing the most highly oxidized component. The major conclusion of Gooding and Muenow (1986) is that the melt pockets formed in an atmosphere that was sufficiently oxidizing to form sulfate from sulfide and that some of the sulfate is present as sulfur-rich, aluminosilicate mineraloids, possibly representing relict grains of Martian weathering or alteration products. Both studies indicate that at least some of the material in the EET 79001 melt pocket is extraneous.

At the time of earlier studies (e.g., Bogard et al., 1986, 1989; Wiens and Pepin, 1988), it was not known whether shock energy could be concentrated sufficiently to produce mm- and cm-size glassy areas within a matrix of sample shocked to only 35–45 GPa (e.g., McSween and Jarosewich, 1983; Schaal and Hörz, 1977). A number of recent studies, highlighting the importance of open (void or pore) space in shocked target rock for concentrating shock energy, support *in situ* formation. Beck et al. (2007) tested a model for melt pocket formation by compaction of porous space in Martian target rocks during passage of a shock front. Collapse of the pore space gives rise to a local pressure spike of short duration as well as anomalously high temperatures (2000–2500 K) compared to the host rock (400 K). The pressure drops rapidly after the pore space has been compacted, while the concomitant temperature decrease is controlled by thermal diffusivity. In this model the pores are connected to, and in equilibrium with, the Martian atmosphere. Shock pyrometry experiments (Stewart et al., 2007), support *in situ* formation of melt pockets and show that shock energy can be concentrated sufficiently to melt discrete areas within the matrix of a sample shocked to pressures >13 GPa. These local hot spots correlate with open pore spaces and cracks at the sample free surface.

Dynamic crystallization experiments alone do not present a unique model for the formation of melt pockets; however, they do set many limits on models. For example, by establishing the crystallization characteristics of melt pockets, parameters such as the amount of heat, the rapidity with

which it is generated, and the rapidity with which it is dissipated, can be characterized, providing a crucial step in developing a workable model. Earlier melt pocket crystallization studies used homogeneous starting material of Los Angeles, Dar al Gani (DaG) 476 and Sayh al Uhaymir (SaU) 150 melt pocket compositions (Walton et al., 2006). The melt pockets investigated were characterized by microporphyritic textures of dendritic (disequilibrium) crystals set in a glassy groundmass, which lacked abundant visible nucleation sites (e.g., schlieren, vesicles, entrained host rock clasts). The experiments were conducted assuming that the melt pockets formed by cooling of what was originally a superheated melt (i.e., liquid free of nuclei). The results showed the best fits for cooling rates in the range 1040–1560 °C/h (Los Angeles) and 780 °C/h (DaG 476 and SaU 150). The duration of the heating event was found to be on the order of minutes (12–16 min) in a small, decimeter-size meteoroid. A small meteoroid size (decimeter vs. meter) is consistent with previous estimates based on terrestrial impact ejecta dimensions (Pohl et al., 1977; Stöffler and Ostertag, 1983), isotopic compositions of Martian meteorites (Eugster et al., 2002), mass loss by ablation in Earth's atmosphere (Ceplecha et al., 1993; Bland and Artemieva, 2003), and numerical modeling of solid particles during launch through the Martian atmosphere (Artemieva and Ivanov, 2004).

It has been observed that melt pockets display a range of textures that is variable between unpaired meteorites and individual melt pockets in a single meteorite (e.g., Walton and Spray, 2003). Broadly, melt pocket textures can be grouped as glassy (schlieren-rich), radial and/or microporphyritic, both containing variable proportions of entrained host rock clasts, immiscible sulfide spheres and vesicles/vugs. Melt pockets possessing microporphyritic textures with equant, euhedral (equilibrium) crystal shapes have been described for lherzolitic basaltic Martian meteorites Lewis Cliff (LEW) 88516, Northwest Africa (NWA) 1950 and ALH 77005 (e.g., Treiman et al., 1994; Walton and Herd, 2007). An earlier survey of melt pockets in ALH 77005, and the similar NWA 1950 meteorite, found that melt pockets possessing microporphyritic textures were common to both meteorites, and were a typical texture observed within melt pockets of a single thin section (Walton and Herd, 2007). In addition, all larger (mm-size) melt pockets in both meteorites are olivine-saturated. The olivine-rich microporphyritic melt pocket investigated in this study is thus regarded as representative of shock melt pockets in the ALH 77005 meteorite, and results may be applicable to melt pockets in other lherzolitic shergottites.

The importance of heterogeneous nucleation on the development of texture has been demonstrated for a wide variety of rock types, including, but not limited to, impact melts (Lofgren, 1977), terrestrial basaltic rocks (Lofgren, 1983), lunar basalts (Lofgren et al., 1974, 1979; Usselman and Lofgren, 1976; Bianco and Taylor, 1977; Grove and Beaty, 1980) and porphyritic pyroxene and olivine chondrules (Lofgren and Russell, 1986; Lofgren, 1989). In this study, we investigate the development of microporphyritic texture in starting material with a composition matching that of a melt pocket in ALH 77005, as a function of variable nucleation sites present at the onset of cooling. Previous studies have sought to develop crystallization scenarios for one textural type of melt pocket (e.g., dendrites embedded in glass; Walton et al., 2006). This study expands on this earlier work to include melt pockets possessing equilibrium- and disequilibrium-shape microphenocrysts with variable nucleation densities (number of crystals per unit volume). Variations in nucleation sites include the number, distribution and kinds of nuclei. The results are discussed in the context of nucleation theory.

This study is primarily concerned with texture. It is thus useful to define the terms used to describe experimental run products. Microporphyritic textures are defined as crystals, too small to be visible to the unaided eye, embedded in a finer-grained or glassy groundmass. Radial textures described for olivine and pyroxene chondrules (e.g., Lofgren and Russell, 1986 and references therein), are defined as radiating dendritic crystals in silicate glass. Here, experimental run products are described from two-dimensional cross sections as viewed in polished block mounts, which were sectioned in a consistent orientation (approximately parallel to vertical; see Section 3). The term "equilibrium-shape" is used to describe equant, euhedral crystals in the run products. Here, "equilibrium" refers to crystals with compact shapes and planar interfaces, and does not imply chemical equilibrium in the system.

2. PETROGRAPHY OF ALH 77005 MELT POCKET

A melt pocket, $\sim 1.9 \times 1.7$ mm, was identified in ALH 77005, 122 as part of a survey of localized melt features in this rock (Walton and Herd, 2007). The melt pocket resides within a poikilitic portion of the rock, consisting of cumulate olivine and chromite enclosed by low-Ca pyroxene. Olivine crystallites occupy 75% of the melt pocket by volume. The remaining 25% is divided between chromite (3%), vugs/vesicles (4%) and host rock clasts (8%) embedded in a glassy groundmass (10%). In hand specimen, the melt pocket has an irregular shape with smaller pockets and veins of melt material emanating from the main melt pocket (Fig. 1a). The main pocket is characterized by a microporphyritic texture of olivine and chromite crystals embedded in silicate glass with minor feathery crystals of clinopyroxene. The microphenocrysts exhibit two distinct shapes: equant euhedral (equilibrium-shape) and skeletal (disequilibrium-shape). Crystal shape changes as a function of distance from the melt pocket center (melt pocket diameter/2) to margin (contact with the host rock). Texturally, the central portion of the melt pocket is dominated by olivine with elongate skeletal shapes (hopper and chain, 5–30×100–450 μm) (Fig. 1b). With proximity to the melt pocket margin (~200 μm) equant hopper olivine shapes become dominant, which in turn grades to a zone of equant, euhedral grain shapes within 10–30 μm distance from the margin (Fig. 1c–e). The transition from elongate skeletal and chain olivine to equant hopper crystals and finally equant euhedral shapes is not well defined, giving rise to broad textural zones. Chromite, entrained within the melt pocket near the margin (tens of microns), has reacted with the melt forming a mottled, recrystallized texture retaining the overall shape of the original chromite grain. Mottled,

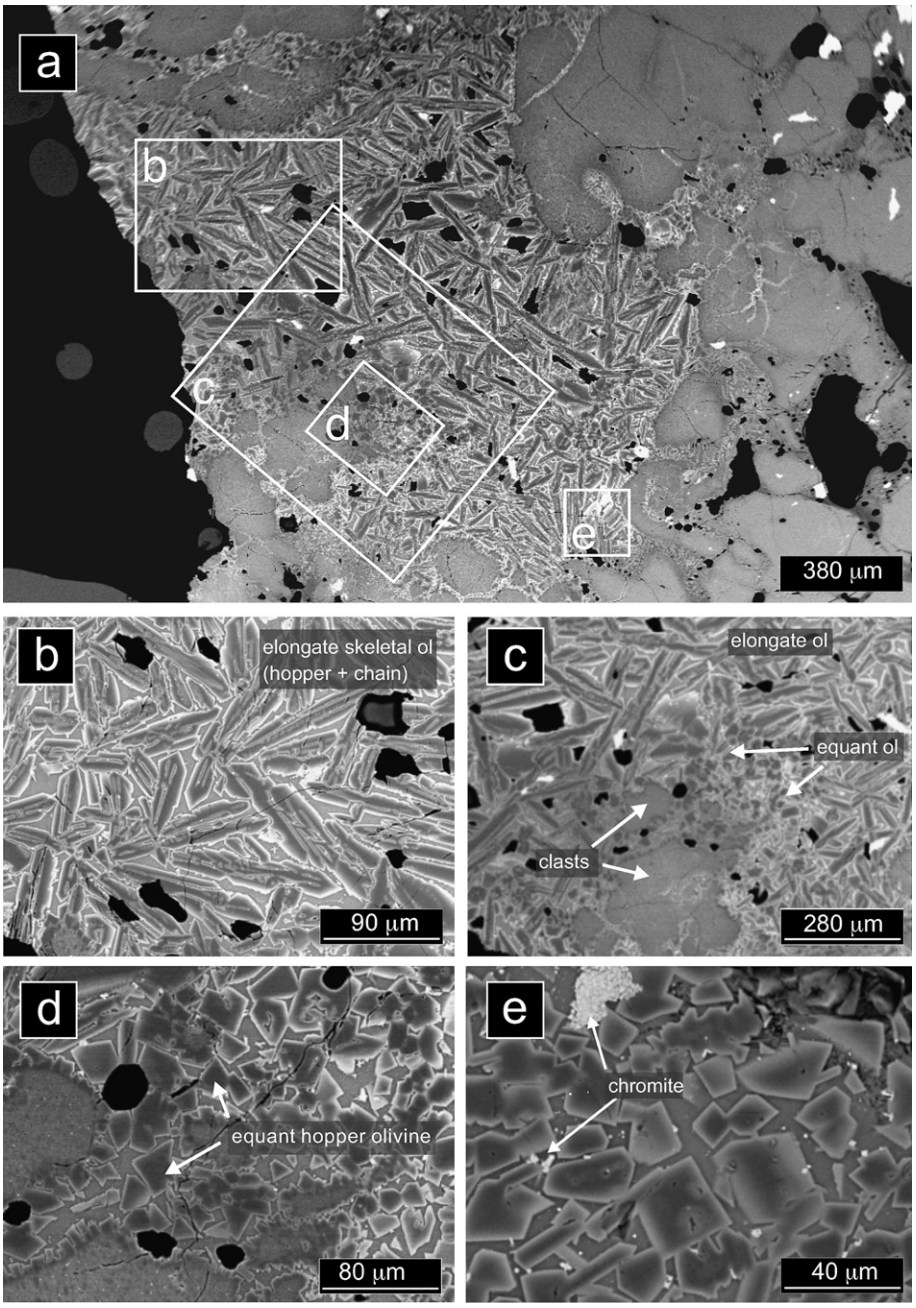

Fig. 1. BSE images of the ALH 77005 melt pocket used as the basis of this study. (a) Melt pocket overview. (b) Elongate skeletal olivine in the melt pocket interior. (c) As the melt pocket margin is approached, elongate skeletons give way to equant hopper and euhedral shapes. The host rock margin is also marked by an increase in abundance of clasts. Vesicles and vugs appear black in the image. (d) Higher magnification image of equant hopper and euhedral olivine near the melt pocket margin (bottom left corner). (e) Olivine and chromite near the melt pocket margin.

recrystallized chromites are lacking in the melt pocket center; instead, small (1–3 μm-size) chromite euhedra and dendrites are disseminated throughout the melt pocket. Olivine adjacent to the melt pocket exhibits a recrystallized granular texture and the transition to microporphyritic textures marks the melt pocket margin. Clasts of olivine have been entrained within the melt pocket, located in close proximity to the margin. These clasts also exhibit a granular texture with olivine euhedra nucleating from the clast margin into the melt pocket groundmass. Textures of ALH 77005, 122 melt pockets, as well as melt pockets from a small chip (,198), have been described by Walton and Herd (2007). The melt pockets in these two samples exhibited exclusively microporphyritic textures; however, a range of microphenocryst shapes was observed including dendritic, elongate skeletal and equant euhedral in the melt pocket center.

3. EXPERIMENTAL TECHNIQUES

3.1. Cooling experiments

The bulk composition of one microporphyritic olivine melt pocket (MPO-1) in ALH 77005, 122, determined by averaging scanning electron microscopy (SEM) energy-dispersive spectrometry (EDS) raster scan analyses in separate areas of 20×26 μm of the melt pocket (see Walton and Spray, 2003 for analytical details), is given in Table 1. This method has been used previously to reproduce bulk shock melt compositions in Martian meteorites (Walton et al., 2006). These data were obtained at the University of New Brunswick using JEOL 6400 digital SEM with an EDAX Phoenix X-ray microanalysis system equipped with a Sapphire Si(Li) detector and Genesis microanalysis software. SEM analyses were obtained with count times of 60 s, beam conditions of 15 kV and 1.5 nA at a working distance of 14 mm. Analyses were calibrated using a multi-element standard block (Type 202-52) produced by the C.M. Taylor Corporation of Sunnyvale, California. Twenty grams of synthetic glass, representative of the bulk composition of MPO-1, were produced from high purity oxides and carbonates by mixing in an agate mortar and pestle for 20 min under acetone. To compensate for Fe-loss to the platinum wire, an additional 5 wt% of the total FeO was added to the starting composition. After weighing and mixing, each sample was dried at 120 °C for 12 h and then fused in air in a Fe-doped Pt crucible at 1550 °C for 6 h. After the initial fusion, each sample was crushed and refused to ensure homogeneity. The resultant glasses were ground to a powder in an agate mortar.

The composition of the starting material was verified by electron microprobe analysis of glass. The bulk composition of the starting products suffered minor losses of FeO and Na_2O during melting, compared to the bulk composition of the melt pocket (Table 1). The powdered starting material was pressed into pellets of ~0.2 g and sintered onto platinum wire loops hung from a ceramic rod containing a thermocouple, located within 2–3 mm of the sample and calibrated against the melting point of gold. Oxygen fugacity was controlled using a mixture of CO and CO_2 gas, and measured with a zirconia cell located in an external reference furnace. The zirconia cell was calibrated using known CO/CO_2 mixtures.

Table 1
Composition of starting material

Oxide	Melt pocket 1	
	Calcd	Measured
SiO_2	38.9	39.3
TiO_2	0.7	0.7
Al_2O_3	4.6	4.7
Cr_2O_3	1.6	2.1
FeO	22.3	21.2
MnO	0.6	0.6
MgO	25.9	26.3
CaO	3.7	3.8
Na_2O	0.9	0.2
P_2O_5	0.7	0.7
Total	99.9	99.6
Liq. T		1510 °C
Liq. phase		Olivine

Liq. T, liquidus temperature; Liq. phase, liquidus phase.

Experiments were conducted as both controlled cooling runs, designed to duplicate the crystallization of the melt pocket, and isothermal runs, designed to approach equilibrium. For each experiment, the sample was introduced into the furnace at T_o and the CO–CO_2 gases were emitted into the furnace within 1 min. The near liquidus melting relations were determined for MPO-1 from the isothermal experiments with melt times varying from 1 to 2 h near the liquidus to up to 24 h at increasingly subliquidus temperatures. Melt temperatures (1520–1560 °C) resulting in glassy run products (100% glass or glass with minor local areas of spherulitic olivine) were interpreted as superliquidus. The liquidus temperature of MPO-1 is 1510 °C, based on the observation that no crystals were observed in runs higher than this temperature, and all runs equal to or less than this temperature contained crystals. Subliquidus conditions (1460–1500 °C) contained abundant crystals upon quenching. The solidus temperature of MPO-1 was determined by a series of isothermal runs, performed over the range 1280–1380 °C in intervals of 10 °C. The solidus temperature was confirmed by a reversal experiment in which the run was started just above the solidus (where melt exists) and then decreased to a temperature below the solidus and held for 24 h to allow crystallization. The run did not contain glass or zoned crystals upon quenching in water, establishing equilibrium. The solidus temperature of MPO-1 is 1295 °C. The starting temperatures of experiments varied from superliquidus ($T_o = 1520$ and 1560 °C), liquidus ($T_o = 1510$ °C) and subliquidus ($T_o = 1460$ and 1500 °C) to observe the effect of heterogeneous nucleation (those runs containing crystals at the onset of cooling compared to those free of crystals) on the crystallization run products (Table 2), following the experimental technique of Lofgren and Russell (1986). The oxygen fugacity of these experiments was equivalent to the fayalite–magnetite–quartz (FMQ) buffer (Wones and Gilbert, 1969).

For the controlled cooling runs, the charges were first held at T_o for 30 min, and then cooled to 1380 °C using a Eurotherm controller, at a fixed rate (ΔT 10–1000 °C/h; Table 2). When the terminal temperature was reached the gases were switched off and the sample removed from the furnace and cooled in air to room temperature. To assess the additional effect of oxygen fugacity on crystallization of the ALH 77005 melt pocket, an additional set of experiments were conducted for $T_o = 1510$ °C, and cooled at a rate of 500 °C/h to 1380 °C. Redox conditions were equivalent to 2 log units below the FMQ buffer (FMQ − 2), as well as FMQ − 1, FMQ, FMQ + 1 and FMQ + 2.

Although the natural melt pockets most likely cooled to ambient temperatures, rather than experiencing quenching above the solidus, the runs were quenched at 1380 °C to shorten the length of the experiments. We postulate that the rapid cooling rates involved in this study, when cooled to subsolidus temperatures (>1295 °C), would still result in some glass present, due to insufficient time for complete

Table 2
Textural description of crystallization run products for MPO-1 at varying cooling rates and fO_2 = FMQ buffer

	Melt 1560 °C	Melt 1520 °C	Melt 1510 °C	Melt 1500 °C	Melt 1460 °C
Melt and quench	Soak: 60 min Run product: 100% glass	Soak: 60 min Texture: Glassy, local areas of spherulitic olivine	Soak: 60 min Texture: microporphyritic Run product: olivine (euhedral), chromite (vermicular) Crystal size: olivine (25–85 μm), chromite (8–12 μm)	Soak: 360 min Texture: microporphyritic Run product: olivine (euhedral) chromite (euhedral) Crystal size: olivine (40–120 μm), chromite (12–25 μm)	Soak: 1440 min Texture: microporphyritic Run product: olivine (anhedral), chromite (euhedral) Crystal size: olivine (50–95 μm), chromite (6–12 μm)
10 °C/h	Duration: 1080 min Texture: microporphyritic Run product: olivine (dendritic[a]), chromite (dendritic/feathery) Crystal size: olivine (1.5–2 mm length), chromite (4–14 μm)	Duration: 840 min Texture: microporphyritic Run product: olivine (elongate skeletal), chromite (vermicular) Crystal size: olivine (700–1100 μm), chromite (2–16 μm)	Duration: 780 min Texture: microporphyritic Run product: olivine (equant skeletal), chromite (vermicular) Crystal Size: olivine (30–88 μm), chromite (8–20 μm)	Duration: 720 min Texture: microporphyritic Run product: olivine (equant, euhedral) chromite (subhedral) Crystal size: olivine (50–150 μm), chromite (8–12 μm)	Duration: 480 min Texture: microporphyritic Run product: olivine (equant, euhedral), chromite (subhedral) Crystal Size: olivine (20–65 μm), chromite (7–12 μm)
500 °C/h	Duration: 22 min Texture: Radial Run product: olivine (dendritic), chromite (dendritic/feathery) Crystal size: olivine (1.8–2.2 mm length), chromite (2–16 μm)	Duration: 17 min Texture: microporphyritic Run product: olivine (elongate skeletal), chromite (vermicular) Crystal size: olivine (500–900 μm), chromite (2–18 μm)	Duration: 16 min Texture: microporphyritic Run product: olivine (elongate skeletal), chromite (vermicular) Crystal size: olivine (50–100 μm), chromite (10–14 μm)	Duration: 14 min Texture: microporphyritic Run product: olivine (equant, euhedral[b]), chromite (anhedral) Crystal size: olivine (80–200 μm), chromite (8–14 μm)	Duration: 10 min Texture: microporphyritic Run product: olivine (equant, euhedral), chromite (anhedral) Crystal size: olivine (18–65 μm), chromite (6–12 μm)
1000 °C/h	Duration: 11 min Texture: Radial Run product: olivine (dendritic), chromite (dendritic/feathery) Crystal size: olivine (1–2.5 mm length), chromite (2–20 μm)	Duration: 9 min Texture: microporphyritic Run product: olivine (dendritic), chromite (vermicular) Crystal size: olvine (500–2000 μm), chromite (3–20 μm)	Duration: 8 min Texture: microporphyritic Run product: olivine (elongate skeletal), chromite (vermicular) Crystal size: olivine (35–100 μm), chromite (8–12 μm)	Duration: 7 min Texture: microporphyritic Run product: olivine (euhedral and dendritic), chromite (vermicular) Crystal size: olivine (30–80 μm), chromite (10–22 μm)	Duration: 5 min Texture: microporphyritic Run product: olivine (euhedral and dendritic) Crystal size: olivine (10–70 μm), chromite (5–16 μm)

Soak, time held at melt temperature. Duration, duration of the cooling interval, not including the soak time at the initial melt temperature.
[a] Olivine dendrites in run 1560 °C, 10 °C/h are randomly-oriented, compared to radial textures with faster cooling from the same melting temperature.
[b] A few equant skeletal (hopper) olivine crystals are observed.

crystallization, in contrast to subsolidus isothermal runs. To test this, we cooled two runs at rates of 500 °C/h and 1000 °C/h from temperatures of 1520 °C and 1500 °C, respectively, to a temperature of 1280 °C. At the terminal temperature the samples were pulled out of the furnace and quenched in air. The run products are compared to the experiments quenched in air at 1380 °C, to determine any difference in crystal shapes produced by quenching above and below the solidus (within a 100 °C range).

The runs in this study were quenched in air to avoid sample loss during drop-quenching in water, by the run sticking to the furnace tube or the platinum wire not fully melting. However, it is well known that rampant quench crystallization can occur during the seconds it takes for a sample cooled in air to reach the glass transition temperature. For example, the 1 bar study of McKay et al. (2004) on the Yamato 980459 bulk composition found that the high liquidus temperature and olivine-rich composition invariably resulted in the formation of quench crystals during air cooling. The bulk composition of MPO-1 used in this study is even more mafic than Yamato 980459. We maintain that the cooling rates involved in air quenching should produce only very fine-grained, feathery crystallites that should be distinguishable from crystals grown during controlled cooling. We carried out water-quenched replicates of runs in order to verify that air-quenching did not adversely affect the resulting run product textures. These additional runs had starting temperatures of 1560, 1510 and 1460 °C and were cooled to 1380 °C. The drop-quenched runs were performed for the fastest cooling rates only, as the goal of these experiments is to distinguish between textures produced by the controlled cooling rate

(1000 °C/h) and quench crystallization occurring during the seconds it takes for a sample to cool in air.

3.2. Sample preparation and analysis

After quenching, the samples were mounted in epoxy. Due to the high melting temperatures (T_o 1460–1560 °C) the platinum loop tended to droop when placed in the furnace hot spot. Crystals formed during the isothermal melting period settled to the bottom of the loop and runs were sectioned in the same orientation, parallel to the loop, to preserve the settled crystals. Not all wire loops drooped depending on temperature and run duration and these runs were sectioned perpendicular to the loop. The resultant thick sections were polished to 0.05 μm finish and carbon-coated in preparation for SEM and electron microprobe (EM) analysis at the University of Alberta. Backscattered electron (BSE) images were obtained using JEOL 6301F Field Emission (FE-) SEM at a working distance of 8 mm and an accelerating voltage of 20 kV. Mineral phases were analyzed using JEOL 8900 microprobe equipped with five wavelength dispersive spectrometers using an accelerating voltage of 15 kV and a beam current of 15 nA. Ferric iron in chromite was calculated on the basis of stoichiometry (Carmichael, 1967). Glasses were analyzed under the same operating conditions as minerals, but with a defocused beam diameter of 5–10 μm. Natural minerals were used as standards and the data was reduced with ZAF correction scheme.

4. EXPERIMENTAL RESULTS

4.1. Melting relations

For the purposes of this study, it is important to constrain the phases present at the initiation of cooling and their effect on the subsequent crystallization of the liquid. The starting composition is given in Table 1. The melting relations for the simple ternary system SiO_2–Al_2O_3–MgO are consistent with experimental results (Davis and England, 1964), where forsterite ($Fo_{88–94}$) is the first phase on the liquidus at 1510 °C at 1 bar. Chromite appears at ~1500 °C, and the solidus temperature is 1295 °C. In the following sections all crystal shapes described from experimental run products refer to olivine, unless otherwise indicated.

4.2. Texture of run products

The duplicate experiments, quenched in water at 1380 °C and subliquidus conditions, show the same olivine and chromite crystal shapes for microphenocrysts observed in air-quenched runs at 1380 °C (~100 °C above the solidus). The runs cooled at 10–1000 °C/h to subsolidus temperatures still contain melt which quenches to glass because the liquidus temperature is over-stepped (undercooled) before nucleation and crystal growth occurs (disequilibrium crystallization conditions). The main difference between duplicates is the presence of ubiquitous feathery crystallites (olivine, clinopy-

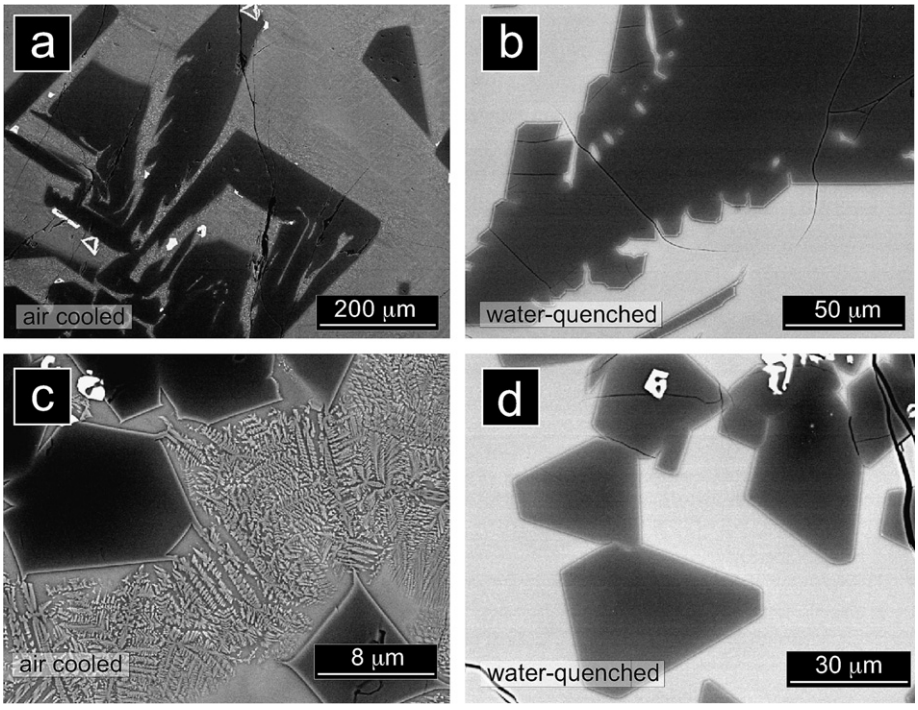

Fig. 2. BSE images of experimental run products showing the difference between runs quenched in air (a, c) and those quenched in water (b, d). Experimental conditions of the runs are 1510 °C, 1000 °C/h (a, b) and 1460 °C, 1000 °C/h (c, d). Air-quenched runs are characterized by ubiquitous feathery crystallites dispersed throughout the groundmass, nucleating from the margins of earlier-formed crystals. Run products quenched in water do not contain quench crystallites and their groundmass is glass. The crystal shape of olivine, the first phase on the liquidus, is not affected by air-quenching. In all four images the dark phase is olivine and the white phase is chromite.

roxene and chromite) in the groundmass of the air-quenched runs (Fig. 2a and c). These feathery crystals are also observed to nucleate from the edges of earlier-former crystals and are interpreted to have formed during the seconds it takes for a run extracted from the furnace, and quenched in air, to reach the glass transition temperature. These quench crystals are easily distinguished from those formed during controlled cooling. The groundmass of water-quenched runs is a crystallite-free glass (Fig. 2b and d). The duplicates show that extracting the runs from the furnace at ~100 °C above the solidus and allowing the run to quench in air does not affect the textures that are the subject this study. Having addressed this issue, the following sections report results and interpretations of the run products for the air-quenched (1380 °C) experiments only.

A variety of olivine microphenocryst shapes were observed: dendritic, skeletal and equant euhedral (Fig. 3 and Table 2). Microporphyritic textures dominate the run products. In this study, the sectioned run products are divided into different zones (bottom, central and upper), resulting from gravitational settling of crystals during the experiment. Bottom zones are interpreted as crystals formed during the initial isothermal melting period of the experiment, settling to the bottom of the charge. Crystals in the central zones are interpreted to be the product of crystal growth, formed under controlled cooling conditions during the experiment (10, 500 and 1000 °C/h). The upper quench zone is developed in the controlled cooling experiments, and consists of feathery crystallites in the air-quenched runs and crystal-free glass in the water-quenched runs; this zone is interpreted to have formed during quench (see previous paragraph). This study is primarily concerned with the textures formed as a result of the experimental growth conditions, and only crystals from the central zone are described and interpreted (Table 2). It should be noted that the runs containing skeletal and radial shapes do not exhibit crystal settling. Crystal settling was observed in subliquidus runs only, as observed in previous experiments (DeHart and

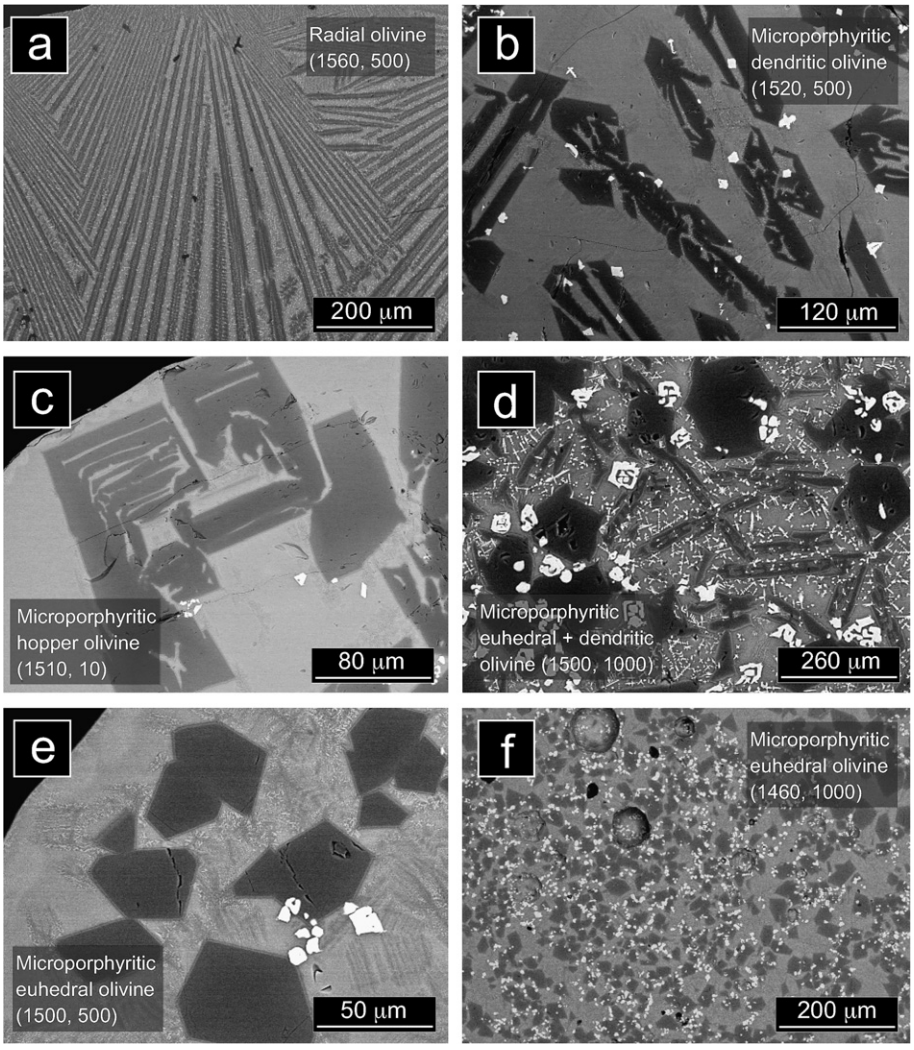

Fig. 3. BSE images illustrating the various microphenocryst shapes produced in dynamic crystallization of ALH 77005 melt pocket composition starting material. The melt temperature and cooling rate are shown separated by a comma. For example, in (a) 1560, 500 denotes a run cooled at a rate of 500 °C/h from a melting temperature of 1560 °C.

Lofgren, 1996). The lack of crystal settling in superliquidus runs is regarded as a result of the nucleation history, rather than a problem with sectioning.

4.3. Textural variations

The texture of runs cooled from melts heated above liquidus temperatures differ markedly from runs cooled from liquidus and subliquidus temperatures. Experiments melted at superliquidus temperatures (1560 and 1520 °C) possess crystal shapes indicative of rapid growth. Radial olivine textures have been produced in the highest temperature runs (1560 °C, ΔT 500–1000 °C/h), comprised of radiating chain olivine crystals in glass (Fig. 3a). When cooled at a slower rate (10 °C/h), the same superliquidus run produced olivine dendrites with random orientations. Runs cooled from temperatures slightly above the liquidus (1520 °C) appear to be most sensitive to the cooling rate parameter, producing the largest variety of olivine shapes, ranging from elongate dendrites at the fastest cooling rate (1000 °C/h; Fig. 3b), to elongate skeletal at moderate cooling rate (500 °C/h), to elongate skeletal with a few equant skeletal (hopper) crystals in the slowly cooled run (10 °C/h). Superliquidus run products are characterized by a low nucleation density (assuming each crystal represents growth of a single nucleus), with a relatively large crystal size (250–2500 μm) (Table 2). Chromite is present as feathery crystallites (1–3 μm) in the groundmass glass (1560 °C) and as coarser (5–20 μm) grains with a vermicular texture in runs melted and cooled from 1520 °C (Fig. 4a and b).

Melts cooled from the liquidus temperature (1510 °C) yielded skeletal crystals ranging from equant to elongate forms with increasing cooling rates (Fig. 3c). The groundmass contains acicular, feathery clinopyroxene crystallites embedded in glass that formed during air quenching. Chromite has a vermicular texture in runs carried out at FMQ (Fig. 4b), but displays different forms depending on oxygen fugacity (discussed below).

Subliquidus melting conditions (1500 and 1460 °C) yielded dominantly microporphyritic textures with equant, euhedral olivine microphenocrysts when cooled at slow to moderate rates (10–500 °C/h; Fig. 3e and f), with the exception of hopper crystals observed in the 1500 °C run cooled at 500 °C/h. Fast cooling (1000 °C/h) from subliquidus temperatures yield transitional run product textures characterized by dendrites nucleating from the corners of equant euhedra, embedded in a glassy groundmass (Fig. 3d). Chromite shapes change from vermicular at 1510 °C to subhedral and anhedral at lower melting temperatures (1500 °C and 1460 °C; Fig. 4b–d and Table 2).

The effect of oxygen fugacity on crystallization of chromite is evident in the texture of experimental runs cooled from the liquidus temperature (1510 °C) at 500 °C/h between FMQ − 2 and FMQ + 2 (Fig. 5). Low oxygen fugacity (FMQ − 2 to FMQ) runs yield chromite with a small grain size (2–10 μm) with vermicular shapes (Fig. 5a and b). At the upper end of the range (FMQ + 1 to FMQ + 2), chromites are characterized by larger (10–22 μm), more equant and subhedral crystals (Fig. 5c and d). Minute rounded chromite crystals (⩽1 μm) are enclosed

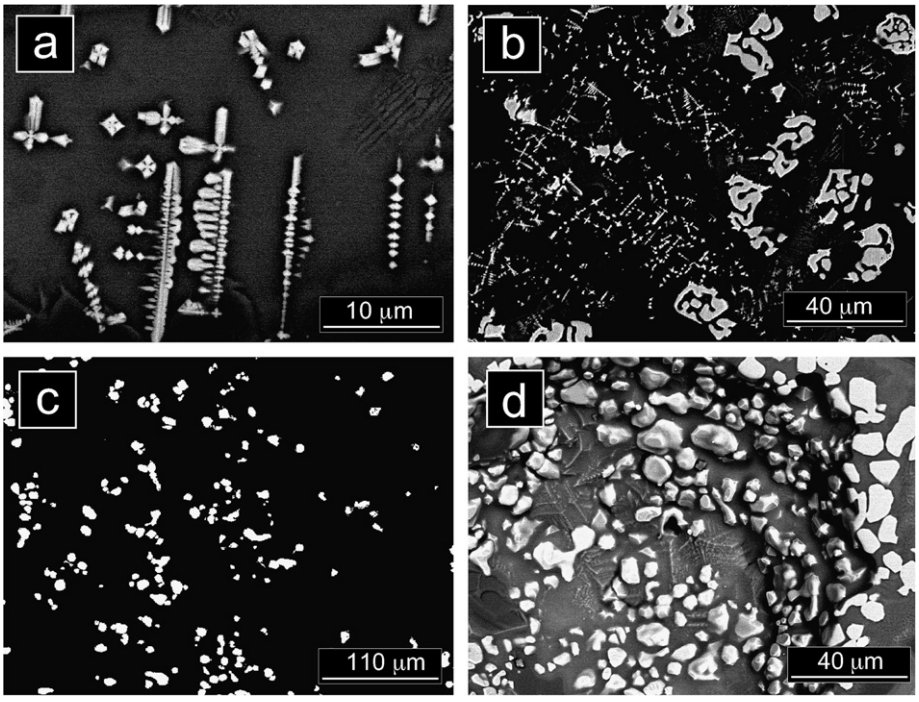

Fig. 4. BSE images of chromite crystal shapes produced over a range of crystallization conditions. (a) Dendritic chromite embedded in silicate glass. (b) Vermicular chromite with fine-grained feathery (dendritic) chromite. The feathery chromite observed in this image forms when the sample is pulled from the furnace and is quenched in air. (c) Anhedral chromite. (d) Subhedral chromite observed in a vesicle in the melt.

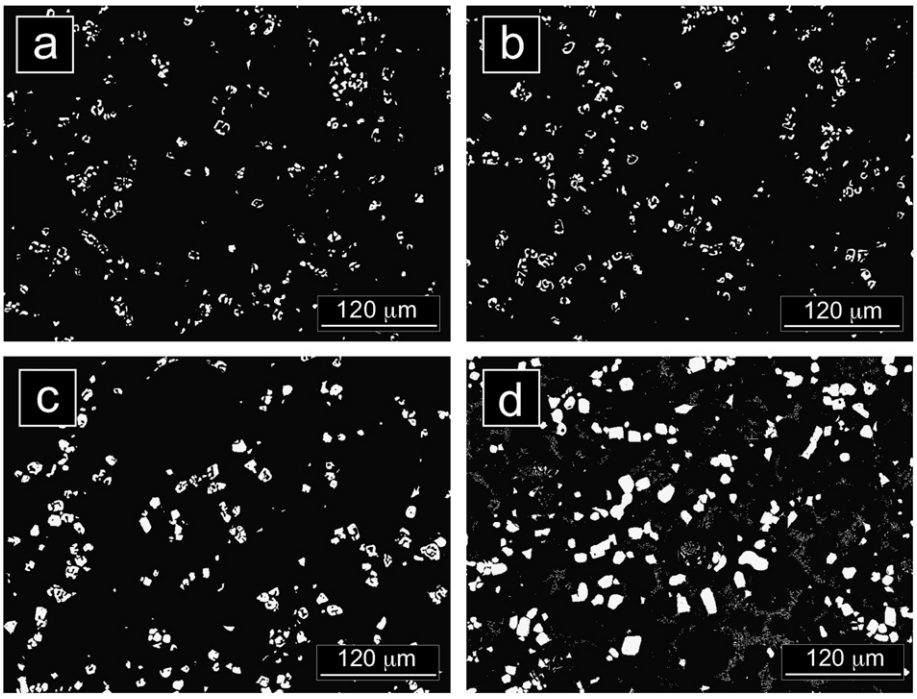

Fig. 5. BSE images of chromite crystals from experimental run products (1510 °C, ΔT 500 °C/h). (a) Chromite crystals formed at FMQ − 2. (b) FMQ − 1. (c) FMQ + 1. (d) FMQ + 2. Note that as fO_2 increases from FMQ − 2 to FMQ + 2, chromite grain size increases and grain shapes become more regularl. Dendrites interstitial to skeletal olivine microphenocrysts have formed in the FMQ + 2 run only (d).

by olivine cores in low-oxygen fugacity runs, indicating that chromite nucleated shortly after olivine under these conditions. In contrast, the euhedral chromite crystals in the high-oxygen fugacity runs are only partially enclosed by olivine rims; this interstitial texture indicates that chromite nucleated later in the run. We attribute the smaller size and vermicular shapes of the chromite grains in the low fO_2 runs to the lower proportion of ferric iron available in the melt, limiting the growth of chromite crystals under these conditions.

4.4. Mineral compositions

Representative analyses from ALH 77005 and MPO-1 run products are given in Tables 3 and 4. ALH 77005 melt pocket microphenocrysts have magnesian cores ($Fo_{71–89}$) with rims zoned to more ferroan compositions ($Fo_{35–57}$). The interstitial glass has an Fe-rich (12.6–13.9 wt% FeO), Al-poor (8.4–9.8 wt% Al_2O_3) basaltic to basaltic andesitic composition. In comparison, analyses from olivine in experimental run products have highly magnesian cores

Table 3
Representative EM analyses of ALH 77005 silicate phases from the natural melt pocket and experimental run products

	Natural melt pocket olivine			Experimental run products[a] olivine			Run products (range of fO_2)[b] olivine			
	Core	Rim	Glass	Core	Rim	Glass	FMQ − 2	FMQ − 1	FMQ + 1	FMQ + 2
SiO_2	40.1	34.1	47.5	39.8	38.5	42.2	38.3	39.6	39.5	40.3
TiO_2	b.d.[c]	0.14	2.33	b.d.	b.d.	5.63	b.d.	b.d.	b.d.	b.d.
Al_2O_3	0.12	0.27	8.4	0.13	0.06	0.94	0.12	0.12	0.09	0.09
Cr_2O_3	0.55	0.15	0.21	0.17	0.15	0.39	0.24	0.15	0.19	0.15
FeO	12.0	42.2	13.1	11.7	20.7	25.5	20.2	13.9	13.5	10.2
MnO	0.26	0.93	0.34	0.42	0.53	0.65	0.49	0.36	0.37	0.31
MgO	46.6	20.6	6.8	47.3	39.7	16.9	40.2	45.8	46.0	48.6
CaO	0.15	0.77	19.5	0.18	0.26	5.4	0.27	0.14	0.18	0.17
Na_2O	b.d.	0.06	0.56	0.05	b.d.	1.39	b.d.	b.d.	b.d.	b.d.
P_2O_5	b.d.	b.d.	1.0	b.d.	b.d.	0.5	b.d.	b.d.	b.d.	b.d.
Total	99.8	99.2	99.7	99.8	99.9	99.5	99.8	100.1	99.8	99.8
Fo	87	40		89	77		78	86	86	89

[a] Run products crystallized under conditions of starting $T = 1510$ °C, $\Delta T = 500$ °C/h and $fO_2 =$ FMQ.
[b] Run products crystallized under conditions of starting $T = 1510$ °C and $\Delta T = 500$ °C/h.
[c] Below detection.

Table 4
Representative EM analyses of ALH 77005 spinel compositions from the natural melt pocket and experimental run products

	Natural melt pocket[a]		Experimental run products[b]							
			FMQ − 2		FMQ − 1		FMQ		FMQ + 1	FMQ + 2
SiO_2	0.60	0.90	0.37	0.28	0.22	0.34	0.18	0.33	0.25	0.21
TiO_2	1.8	2.2	1.2	1.3	1.0	1.5	0.9	1.0	1.0	1.0
Al_2O_3	7.8	17.1	11.3	11.1	10.7	8.1	9.5	8.5	6.3	6.4
Cr_2O_3	50.7	38.4	39.7	31.4	45.2	12.9	43.5	28.2	12.3	12.0
FeO	20.8	27.4	21.6	20.5	18.2	21.9	18.0	22.3	18.2	16.9
Fe_2O_3[a]	5.4	2.2	15.2	24.4	12.8	45.2	16.1	30.0	51.1	51.9
MnO	0.49	0.48	0.41	—	0.43	0.35	0.46	0.41	0.38	0.37
MgO	10.4	8.6	9.8	10.0	11.0	8.5	10.6	8.4	10.5	11.1
CaO	0.13	0.37	0.31	b.d.[c]	0.12	0.07	b.d.	0.15	b.d.	b.d.
V_2O_3	0.35	0.46	—	—	—	—	—	—	—	—
Total	98.5	98.1	99.9	99.0	99.7	98.9	99.2	99.3	100.0	99.9
Usp[d]	0.09	0.11	0.06	0.06	0.05	0.08	0.05	0.05	0.05	0.05
Sp[d]	0.16	0.34	0.22	0.22	0.21	0.16	0.18	0.17	0.13	0.13
Chr[d]	0.68	0.52	0.53	0.41	0.58	0.18	0.57	0.39	0.16	0.16
Mt[d]	0.07	0.03	0.19	0.31	0.16	0.58	0.20	0.39	0.66	0.66

Where two analyses are presented, the first represents the most Cr-rich (primary) and the second, the most Cr-poor (evolved).
[a] Natural melt pocket spinel crystals are dendritic and difficult to analyze, resulting in low totals, greater uncertainties in ferric iron calculation and underestimation of Fe_2O_3.
[b] All run products crystallized under conditions of starting $T = 1510$ °C and $\Delta T = 500$ °C/h.
[c] b.d., below detection.
[d] Usp, ulvöspinel [molar $2Ti/(2Ti + Cr + Al + Fe^{3+})$]; Sp, spinel [molar $Al/(2Ti + Cr + Al + Fe^{3+})$]; Chr, chromite [molar $Cr/(2Ti + Cr + Al + Fe^{3+}$]; Mt, magnetite [molar $Fe^{3+}/(2Ti + Cr + Al + Fe^{3+})$].

($Fo_{89–90}$), zoned to more ferroan rims. The rims of experimental olivine are thinner (<1 μm) compared to the natural crystals (1–2 μm) making quantitative analyses difficult. The most ferroan composition measured is Fo_{71}, much more magnesian than in natural crystals. The interstitial glass in the experiments has an Fe-rich (22.6–28.5 wt% FeO), Al-poor (5.2–7.0 wt% Al_2O_3) basaltic to picro-basaltic composition.

Olivine analyses from natural melt pocket crystallites and experimental run products are compared based on minor element abundances and Mg-number in Fig. 6. Experimental olivine cores are slightly more magnesian than natural melt pocket olivine cores as a result of Fe loss to the Pt loop during the soak stage. MnO exhibits incompatible behaviour and analyses from the experimental olivine fall along the same trends as olivine from the natural melt pocket. Cr_2O_3 abundances are much higher in natural melt pocket crystallites (0.12–0.68 wt% Cr_2O_3) compared to experimental olivine, typically falling within the range 0.09–0.23 wt% Cr_2O_3. For both, Cr_2O_3 contents show a positive correlation with increasing Mg-number, with a slight downturn at the highest Mg-numbers ($Fo_{85–94}$). CaO, like MnO, shows incompatible behaviour. Analyses from experimental olivine fall along the same trend as olivine in the natural melt pocket with higher CaO content at the lower range of Mg-numbers (Fo_{35-60}; 0.21–0.52 wt% CaO) and lower CaO contents at the highest Mg-numbers ($Fo_{>70}$; 0.09–0.21 wt% CaO with a few outlying points).

Walton and Herd (2007) noted two chromite textures within melt pockets in ALH 77005: a mottled, recrystallized texture that retains the overall shape of the original chromite grain, near the margins of the melt pockets; and small (1–3 μm) dendrites within melt pocket cores. The compositions of these chromite crystals are shown in Fig. 7, and compared with those of chromite in the host rock; representative analyses are provided in Table 4. Dendritic chromites extend to more magnesian and aluminous compositions relative to the host rock chromites, having Cr# (=molar Cr/(Cr+Al)) as low as 0.6, and Fe# (=molar Fe/(Fe+Mg)) as low as 0.53 (Walton and Herd, 2007). Experimental chromites as represented by those crystallizing at $T_o = 1510$ °C and cooling at 500 °C/h under variable oxygen fugacity, have Cr# as low as 0.52 and Fe# as low as 0.46, and reproduce the trend of the melt pocket dendrites in extending to more aluminous compositions (Fig. 7).

Chromite analyses from the experimental runs produced under varying oxygen fugacity conditions, in general, show the expected increase in Fe^{3+} with increasing oxygen fugacity; chromites crystallized at FMQ + 2 have upwards of 51 wt% Fe_2O_3. However, chromites from the FMQ − 2, FMQ − 1 and FMQ runs show compositional variability reflecting evolution of the melt (Fig. 8). For each of these redox conditions, chromites evolve from Fe^{3+}- and Ti-poor to Fe^{3+}-rich, with only a modest increase in Ti. Locally within the FMQ − 1 run, chromites evolve to Fe^{3+}-rich compositions comparable to chromites in the FMQ + 1 and FMQ + 2 runs. In general, more oxidized runs yield chromites with a higher molar proportion of magnetite, lower chromite and spinel, with very little change in the ulvöspinel content: FMQ − 2 chromites contain 41 to 58% Chr (=molar $Cr/(2Ti + Cr + Al + Fe^{3+})$), 17–30% Mt (=molar $Fe^{3+}/(2Ti + Cr + Al + Fe^{3+})$), 22–25% Sp

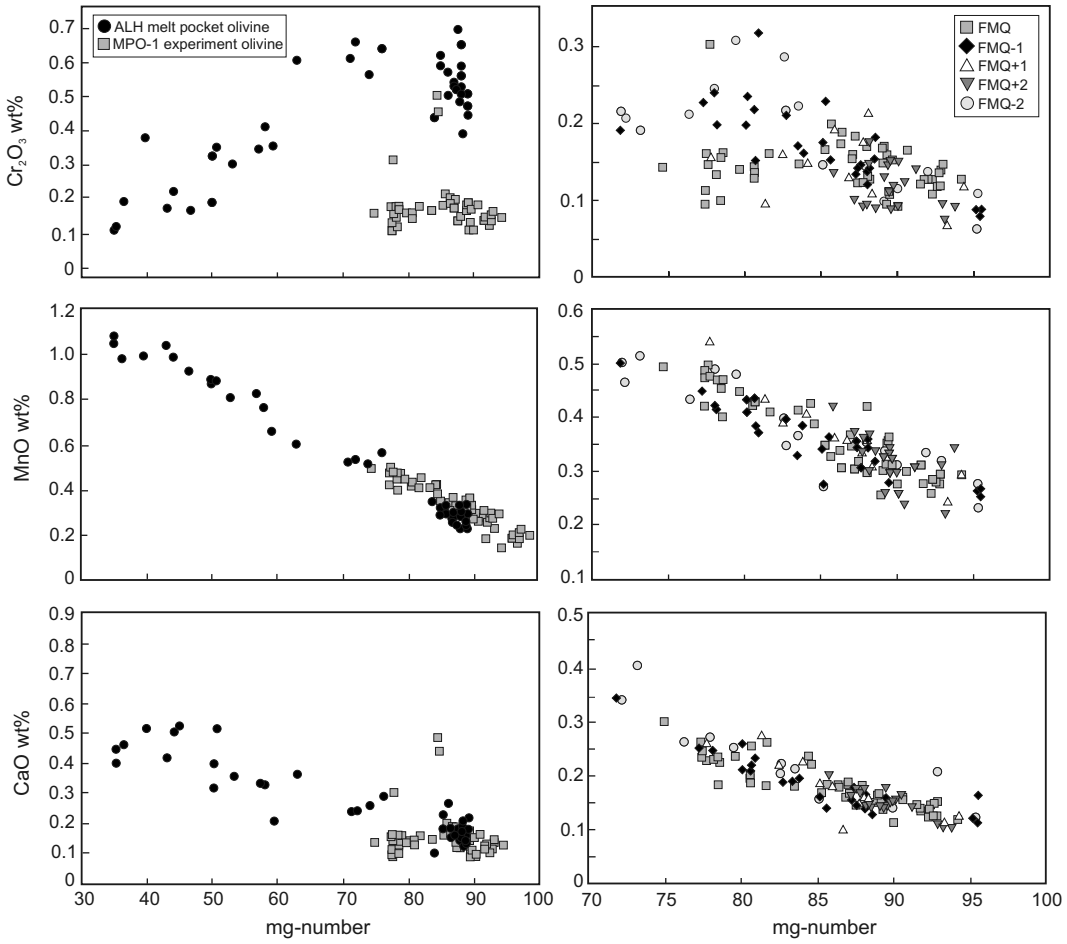

Fig. 6. Variations of Cr_2O_3, MnO and CaO, relative to mg-numbers, in melt pocket olivine from the natural meteorite, and experimental run products produced over a range of cooling rates (10–1000 °C/h) and fO_2 conditions (FMQ, FMQ ± 1, 2) (See text for details).

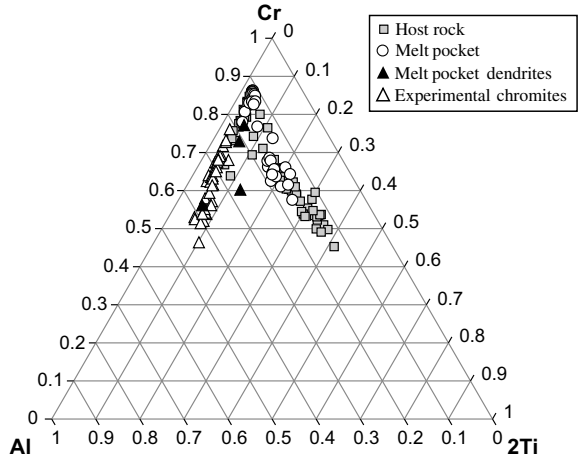

Fig. 7. Comparison of natural with experimental chromite compositions for ALH 77005 in the system chromite (molar Cr/[Cr + Ti + Al])-ulvöspinel (molar 2Ti/[Cr + Ti + Al])-spinel (molar Al/[Cr + Ti + Al]). Melt pocket compositions are those of mottled, recrystallized chromites near melt pocket margins. Melt pocket dendrites are dendritic chromite within melt pocket centers. Experimental chromites are from experiments carried out over a range of oxygen fugacities, as described in the text.

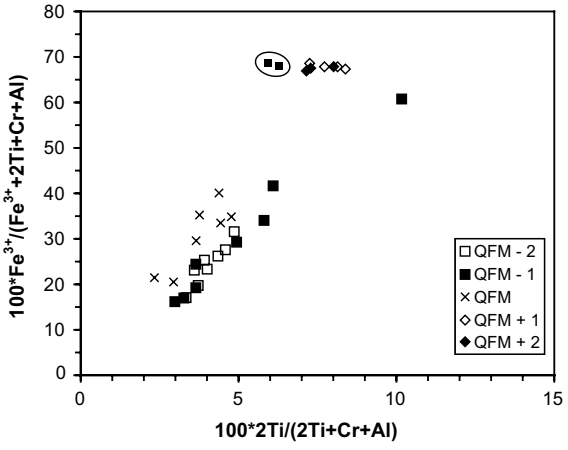

Fig. 8. Variation in composition (magnetite vs. ulvöspinel) of experimental chromite crystallized under different oxygen fugacity conditions. Circled points from FMQ − 1 data represent chromites enclosed by olivine, and presumably crystallized from a more evolved portion of the melt.

(=molar Al/(2Ti + Cr + Al + Fe^{3+})) and 5–8% Usp (=molar 2Ti/(2Ti + Cr + Al + Fe^{3+})); FMQ + 2 chromites contain 16–18% Chr, 66% Mt, 12–13% Sp, and 5 % Usp. The more homogeneous, Mt-rich compositions of the FMQ + 1 and FMQ + 2 chromites are consistent with the inference derived from their textural relationship with olivine (see above) that they nucleated later in the run, from a more evolved melt.

5. DISCUSSION

5.1. An overview of nucleation and crystal growth

Many silicate liquids can be cooled below their equilibrium liquidus temperature without crystallization of the liquidus phase (e.g., Lofgren, 1983). This overstepping provides the energy needed to form a nucleus on which growth can occur, and is called undercooling or supercooling ($-\Delta T$). A nucleus can be thought of as the initial products of crystallization, or, more specifically, as the clustering of various ions in the melt to form the initial structured pattern of a crystalline solid (Gago-Duport et al., 1995). Nucleation and subsequent growth of a crystal can be homogeneous, if it arises entirely through random aggregations of atoms formed due to local, transient supersaturation, or heterogeneous, if the presence of another phase (i.e., crystalline material) in contact with the liquid facilitates growth. For heterogeneous nucleation the presence of an existing phase reduces the surface free energy, which in turn reduces the activation barrier to nucleation. In general, nucleation is a sluggish process requiring heterogeneous nucleation (Uhlmann and Chalmers, 1965; Yinnon et al., 1980; Lofgren, 1983).

An important concept of nucleation is that of the embryonic nucleus (embryo) versus the super-critical nucleus (Turnbull, 1950; Dowty, 1980). An embryo is crystalline material smaller than the critical size required to form a stable crystal nucleus (i.e., a subcritical-size potential heterogeneous nucleus). Embryos usually exist in a melt whether stable nuclei are present or not. If a melt is sufficiently superheated, nuclei and even embryos can be destroyed (Turnbull, 1950). The critical size for nuclei at fast cooling rates is small compared to that of a slowly cooled melt where the nucleation rate is low but the growth rate is rapid (Lofgren, 1983). As the degree of $-\Delta T$ increases, the critical size of a nucleus decreases so that embryos can become nuclei simply as $-\Delta T$ increases during rapid cooling (Lofgren, 1983). When a given embryo reaches critical size, crystallization will begin and the $-\Delta T$ at which growth begins will then dictate the texture.

At temperatures just below the liquidus (near to equilibrium) crystal growth is characterized by the formation of well-faceted crystals. Under these conditions the growth rate is slow, controlled largely by interface attachment kinetics at defects on the crystal face. Of the myriad of collisions at the interface, only a few atoms have the correct velocity, orientation, charge or composition for attachment. At temperatures well below the liquidus (far from equilibrium) the free energy difference between the crystal and the liquid is large enough that interface kinetics are no longer controlling factors and diffusion becomes the rate-determining process (Keith and Padden, 1963; Kirkpatrick, 1975; Dowty, 1980). Thus, as $-\Delta T$ increases the planar interface of a crystal with the melt becomes unstable, resulting in non-compact, highly branching shapes (skeletal, dendritic and radial or spherulitic, Lofgren et al., 1974; Donaldson, 1976; Lofgren, 1980).

5.2. The role of heterogeneous nucleation and cooling rate in ALH 77005 melt pockets

5.2.1. Radial textures

Cooling from the highest melt temperature (1560 °C), yielded textures dominated by large (mm-size) dendritic crystals of olivine embedded in glass with minor chromite. In this case, nucleation sites were reduced to embryos by superheating leaving few, if any, nuclei. The most extreme case produced radial olivine, similar to barred olivine chondrules (e.g., Tsuchiyama et al., 1980; Lofgren, 1989). This cooling history allows for growth of few crystals from embryos, which graduate to nuclei by reducing the critical size for growth by supercooling, resulting in crystals possessing dendritic and/or elongate skeletal shapes. The low nucleation density allows for the crystals to grow large. At slower cooling rates superliquidus runs produce randomly oriented dendritic crystals.

5.2.2. Microporphyritic textures

Runs cooled from temperatures slightly above the liquidus (1520 °C), produce various microphenocryst shapes that range from elongate dendritic to elongate skeletal, at fast to moderate cooling rates. When cooled slowly, run products contain elongate skeletal crystals with a few equant skeletal (hopper) crystals.

Runs cooled from liquidus temperatures (1510 °C) yield microphenocrysts with skeletal shapes, progressing with increased cooling rate, from equant to elongate forms. These textures develop from a melt containing few nuclei, but with abundant embryos graduating to nuclei at low degrees of supercooling.

There is a range of conditions over which microphenocrysts with equilibrium-shapes will form in MPO-1 melts. Subliquidus melts, cooled at moderate to slow rates (10–500 °C/h), contain ubiquitous equant, euhedral crystals. For these runs, nuclei were present at the onset of cooling and crystal growth was immediate at low degrees of supercooling. The size of the microphenocrysts decreases and their number (nucleation density) increases at increasingly subliquidus melt temperatures. The number of crystals present at the time of cooling and their mutual interference (spatial density of nuclei) control crystal size during growth.

Fast cooling from subliquidus temperatures (1500 and 1460 °C) yield transitional run product textures characterized by dendrites nucleating from the corners of equant, euhedral microphenocrysts embedded in a groundmass of glass. For these conditions, nuclei were present in the run at the initiation of cooling and growth was immediate (low degrees of supercooling) giving rise to equant, euhe-

dral shapes dictated by attachment at the crystal-melt interface. Increased cooling caused a change to diffusion-limited growth and the crystals grew with a dendritic shape at large degrees of supercooling. Nucleation takes place at the corners of crystals because these sites form natural protuberances (compared to a crystal face) into the more nutrient-rich melt, away from the growing crystal, which is surrounded by a layer of rejected solutes.

5.3. Comparison of experimental run products and the natural melt pocket

Microphenocryst olivine shapes in the natural melt pocket are equant euhedral, hopper and elongate skeletal, comparing well with representatives from the experimental run products (MPO-1). Radial olivine and transitional textures, produced experimentally in MPO-1, have not been observed in the natural pocket. Elongate skeletal olivine shapes, characteristic of the central portions of the natural melt pocket, have been produced in MPO-1 by crystallizing melts heated to temperatures slightly above the liquidus (+20 °C) at cooling rates of 10 and 500 °C/h, and also by melting at liquidus conditions (1510 °C) and cooling at moderate to fast rates (500 and 1000 °C/h). Equant skeletal (hopper) shapes, characteristic of crystals more proximal to the melt pocket margin, were produced in MPO-1 by slow cooling (10 °C/h) from the liquidus temperature. At a slightly lower temperature (1500 °C) hopper crystals were present when cooled at a modest rate (500 °C/h). The melt pocket margin, characterized by equant, euhedral crystal shapes, shows fits with experimental conditions of subliquidus melting temperatures, cooled at 10–500 °C/h.

It should be noted that the temperature estimates from the experiments are only minimum values, as temperatures could have been much higher but only for a short period of time (seconds to minutes). If melting times are long (hours) then temperatures would have to be subliquidus for preservation of abundant nuclei, however, long melt times are unlikely for shock-produced melts (see following discussion, Section 5.4).

5.4. Cooling history of a melt pocket in the Allan Hills 77005 lherzolitic shergottite

Shock metamorphism is a dynamic process, distinguished from normal geological processes by high strain rates (10^4/s to 10^9/s), transient stress conditions and rapid response times (see French, 1998 for review; Langenhorst, 2002; Sharp and DeCarli, 2006). It is thus expected that the cooling of a melt pocket will take longer than the melting event (by shock) and the duration of cooling will play a larger role in determining the length of the overall melt pocket-forming event. It is therefore important to constrain not only the characteristics of the melt at the start of cooling (presence or absence of nuclei, Sections 5.2 and 5.3), but also the cooling rate of the runs (duration of cooling). This section will focus on constraining the cooling rate of the runs, from which estimates of cooling times can be made. As discussed in the previous section experimental run products show best fits for central melt pocket temperatures of 1510–1520 °C, progressing to a zone heated to 1500–1510 °C and finally the melt pocket margin 1500–1460 °C, cooled over a range of cooling rates 10–1000 °C/h. For crystallization of a melt pocket, moderate to fast cooling rates (500–1000 °C/h), and hence short duration cooling intervals (~8–17 min) are favored over slow cooling (10 °C/h) and hence longer duration events (720–840 min) (Table 2). Textural evidence in thin sections of ALH 77005 to support this include the presence of host rock clasts and schlieren-rich melt pockets, attesting to rapid cooling and solidification, such that the melt was not homogenized during the heating event and clasts were not completely melted and assimilated. Fast cooling is also consistent with the presence of trapped Martian atmosphere (e.g., Bogard and Johnson, 1983; Wiens and Pepin, 1988; Walton et al., 2007) and high-pressure polymorphs (Beck et al., 2004, 2007) in natural melt pockets, requiring rapid freezing of the melt for preservation. Based on the previous lines of evidence, cooling rates in the range 500–1000 °C/h are favored over slow cooling at 10 °C/h. Note that cooling the melt pocket to a subsolidus temperature, rather than quenching 100 °C above the solidus, as employed in this study, will increase the cooling time by a few minutes. However, the main conclusion is that the melt pocket cooled on the order of minutes, not hours, and this result is not changed. A sketch of the natural melt pocket, and the cooling and crystallization history determined in this study, is given in Fig. 9. The experiments show that the final melt pocket texture is most dependent on the starting temperature and cooling rate, rather than the final quench temperature.

5.5. Redox conditions of crystallization of the ALH 77005 melt pocket

Chromite shapes in the core of the natural melt pocket are dendritic, and their compositions are chromite-rich: 52–68% chromite, 16–36% spinel, ~10% ulvöspinel, and a minimum of 5% magnetite (the small size of the crystals resulted in greater uncertainty in these analyses; results of ferric iron calculation by stoichiometry are considered minimum estimates). Of the chromites crystallized in our experiments, those formed at FMQ − 2 are the closest match in terms of crystal shape and composition (41–58% Chr, 22–25% Sp, 17–31% Mt and 5–9% Usp). On the basis of this comparison, and recognizing that the morphology of the crystals is not solely a function of oxygen fugacity, we conclude that the oxygen fugacity of crystallization of the melt pocket cores is consistent with the oxygen fugacity of the host rock mineral assemblage, FMQ − 2.6 (Goodrich et al., 2003). The estimate of Goodrich et al. (2003) is based on olivine-pyroxene-spinel oxybarometry using chromite enclosed in poikilitic pigeonite, representative of the earliest-formed and least re-equilibrated chromite; these chromites have the highest Cr# and lowest Fe# of the chromites in ALH 77005.

The consistency between apparent melt pocket redox conditions and those of the host rock implies that the oxygen fugacity of the melt pocket was set by the Fe^{3+}/Fe^{2+} ratio imparted by the melted host rock material. The

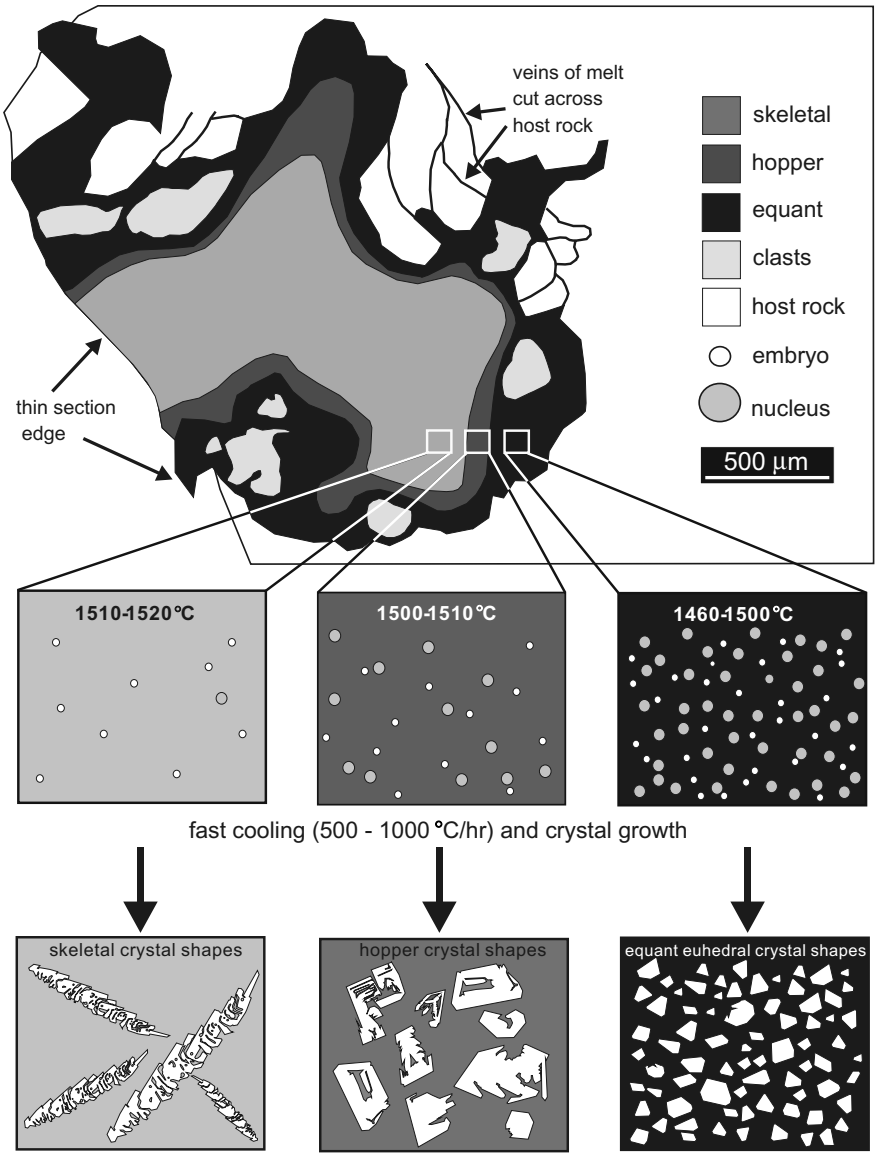

Fig. 9. Sketch of the ALH 77005 melt pocket investigated in this study illustrating the relationship between the presence, distribution and abundance of embryos and nuclei at the onset of cooling, and the resultant texture of the melt pocket. Sketches of crystal shapes in the lower boxes are not shown to scale.

dominant control on the oxygen fugacity of the melt pocket is apparently internal, and external factors, such as the incorporation of CO_2-rich Martian atmosphere (Bogard and Johnson, 1983; Wiens and Pepin, 1988), or oxidized Martian alteration or weathering products (Gooding and Muenow, 1986), have little, if any, influence. Such a conclusion is consistent with observations/arguments demonstrating that the amount of CO_2 dissolved in the melt during the shock event is extremely small, on the order of 13 ppm (Wiens and Pepin, 1988); at such low levels, we would not expect volatiles to have any redox buffering capacity; nor would we expect that dissociation of CO_2 into CO and O_2, and degassing of any of these species woul significantly affect the redox state of the melt. Karner et al. (2006) used determinations of V valence state in Elephant Moraine (EET) 79001 shock glass (Lithology C) to determine that the oxygen fugacity of the glass is within 1 log unit of iron-wustite, equivalent to approximately FMQ − 3. The upper range of their estimates is lower than the oxygen fugacity of the groundmass of Lithology A (FMQ − 1.7 determined by Fe-Ti oxide oxybarometry; Herd et al., 2001), but consistent with the oxygen fugacity of the more reduced xenocryst assemblage within Lithology A (FMQ − 2.8 determined by olivine–pyroxene–spinel oxybarometry; Goodrich et al., 2003). It is unclear what, if any, redox reactions occur during shock to oxidize or reduce Fe, V, or other multivalent elements, or whether such reactions can be elucidated given the non-equilibrium nature of the shock process. Regardless, our favored model of localized, *in situ* shock melting would predict that the oxygen fugacity of the melt pocket is set by the redox state of the material undergoing melting. Comparing the redox states

of melt pocket glasses and mineral phases with those of their host rocks may test such a prediction.

It is thus concluded that the redox state of the Martian atmosphere, and that of the melt pocket in which atmospheric gas is trapped, are decoupled because of the inefficiency of CO_2 uptake, the disequilibrium nature of the shock process, and the dominance of ferrous-ferric buffering due to the higher Fe abundance in the rock relative to any other multivalent element. Although the signature of the Martian atmosphere is present in melt pockets, it appears as though the oxidizing potential of this component is limited. Furthermore, if any alteration or weathering products are incorporated during melt pocket formation, they are in such low abundance, or have such low oxidizing potential as to have little influence on the redox state of the melt pocket.

5.6. Comparison with previous melt pocket crystallization experiments

It has been shown from detailed petrographic studies of Martian meteorite melt pockets that textures are extremely variable between meteorites, between melt pockets in a single meteorite, and even within a single melt pocket. For example, melt pockets in ALH 77005 thin sections and sample chips display a range of textures from melt pockets possessing solely equilibrium-shapes, to melt pockets containing solely skeletal crystals and some containing both crystal shapes and even spherulites (Walton and Herd, 2007). This suggests that that there is a range of temperatures over which melt pockets form in any given meteorite.

Previous crystallization experiments on melt pockets in Martian basalts have shown that these melt pockets cool from post-shock temperatures within minutes (12–16 min) at rates 780–1560 °C/h (Walton et al., 2006). This cooling environment yields randomly oriented dendritic olivine, apatite and clinopyroxene with minor chromite and Fe-oxides in glass. The liquidus temperatures of basaltic meteorite melt pockets ($T_o = 1200$, 1300 and 1455 °C; Walton et al., 2006) are lower than those determined for the more Mg-rich, refractory melt pocket observed in this study ($T_o = 1510$ °C). As a result, melt pockets in Martian basalts tend to form more dendritic textures whereas MgO-rich melt pockets from lherzolitic shergottites have higher melting temperatures and display more microporphyritic textures with microphenocrysts having more skeletal and equilibrium-shapes. This reflects the likelihood that melt pockets with lower liquidus temperatures will be more completely melted.

5.7. Implications for trapped Martian atmosphere and the models for melt pocket formation

The crystallization experiments and compositional data presented in this study shed light on the origin of melt pockets and their cooling history. These results have implications for the interpretation of gas compositions in Martian meteorite melt pockets and constrain cooling times for melt pockets. It has been suggested that melt pockets in Martian meteorites represent Martian regolith that was shock melted and injected into the target rock (Rao et al., 1999), evidenced by isotopic and compositional studies of EET 79001 melt pockets (Wooden et al., 1982; Nyquist et al., 1986; Gooding and Muenow, 1986). The fine-grained, porous nature of the regolith could also account for emplacement efficiencies of gases (Wiens, 1988). However, we find that the scenario of void collapse for local melting and gas implantation is consistent with present knowledge of textural and shock characteristics of Martian meteorites. Specifically, observations of gradational contacts, bulk composition, oxygen fugacity constraints, and recent studies showing the importance of open (void or pore) space for concentrating shock energy, are used to argue for an *in situ* formation mechanism. MPO-1 is in a poikilitic (olivine-rich) area of ALH 77005, and its bulk composition represents an Mg-rich, olivine-saturated melt with a high liquidus temperature as would be expected by local melting of poikilitic areas. The compositions of experimentally produced chromites reproduce the trend of increasing aluminum at constant Ti content in melt pocket chromites (Fig. 7) which extends from the high-Cr#, low-Fe# chromites within the poikilitic portion of the rock. Therefore the melt pocket most likely consists of material derived from the *in situ* melting of the poikilitic portion. The observation that the redox state of the melt pocket is similar to that of the poikilitic portion in which the melt pocket resides represents further evidence for *in situ* melting. If the melt pockets formed by melting and injection of Martian regolith they would be expected to record oxidizing fO_2 conditions, given the oxidizing nature of the Martian surface (e.g., Zent and McKay, 1994; Yen et al., 2000), and the oxidized nature of aqueous alteration products in Martian meteorites, which include ferrihydrite, jarosite and other minerals that formed as a result of interaction with near-surface waters on Mars (e.g., Treiman et al., 1993; Treiman, 2005; Herd, 2006; Vicenzi et al., 2007). Further evidence for the *in situ* formation of melt pockets is the well-documented compositional heterogeneity of melt pockets in a single meteorite, vein on the scale of a single thin section (e.g., Walton and Spray, 2003). The melting and injection model is unlikely to account for the heterogeneity of melt pockets at this scale; nor are the melt pocket bulk compositions consistent with bulk melting of the Martian regolith (see McSween and Keil, 2000 for compiled data). In addition, if melt pockets represent injected material that acquired its atmospheric gases by absorption at the Martian surface, the atmospheric signature would be expected to be restricted to the melt pockets and veins only; however, it has been shown that maskelynite mineral separates also contain small amounts of trapped gases (Bogard and Garrison, 1999; Walton et al., 2007).

We conclude that the presence of Martian alteration or weathering products in melt pockets do not require that Martian regolith was melted and injected into target rock. The results of this study are consistent with melt pockets formed by local *in situ* melting by void collapse, and that their bulk composition and oxygen fugacity records local mineral-scale melting of host rock (meteorite) minerals. In this scenario, the melt pockets would be connected to, and in equilibrium with, the Martian atmosphere, with pos-

sibly alteration/weathering products present inside the cavity prior to collapse.

The results of this study also constrain the duration of the heating and cooling event. From the determined cooling rates, it is determined the melt pockets took ~8–17 min to cool to subsolidus temperatures, consistent with results from previous experiments (Walton et al., 2006). However, Beck et al. (2007) calculate a cooling time of 0.2 s for a 1 mm diameter melt pocket (comparable to the size of the melt pocket in this study). We contend that cooling times of such short duration, effectively quenching the sample, would result in radial textures in the meteorite, which are not observed. Cooling times on the order of minutes are consistent with the natural textures. Models for melt pocket formation, including their heating and cooling history must also take into account the heat sources and heat sinks within the meteoroid, i.e., adjacent melt pockets and veins, shown to be abundant particularly in ALH 77005 (Walton and Herd, 2007) will decrease the magnitude of the thermal gradient after some time because of the interference of their thermal haloes. This will increase cooling time. In addition, the host rock has undergone a post-shock temperature increase (800 ± 200 K for a bulk shock of 45–55 GPa; Fritz et al., 2005), which also acts to increase cooling time. Walton et al. (2006) calculated that for a relatively short cooling duration (16 min) ~20–30% (up to 60%) of argon (a noble gas with a $^{40}Ar/^{36}Ar$ signature that is diagnostic of the Martian atmosphere), can be lost from the melt pocket to the surrounding minerals by diffusion. This will affect the amount of atmospheric gases in the melt pocket, but will not affect recognition of the signature of Martian atmosphere (in terms of isotopic ratios), because diffusion is a non-fractionating process.

6. CONCLUSIONS

Melt pockets are localized shock-generated hot spots in strongly shocked Martian basalts and lherzolitic basalts, presumably formed during the impact event, which launched the rocks into eventual Earth-crossing trajectories. The results of this study constrain the heating and cooling regime for a microporphyritic melt pocket in ALH 77005, as well as the oxygen fugacity of crystallization. Within the melt pocket, strong thermal gradients existed at the onset of crystallization, giving rise to a heterogeneous distribution of nucleation sites at the onset of cooling and crystallization resulting in gradational textures of olivine and chromite. Skeletal olivine in the melt pocket center crystallized from a melt containing few nuclei, which cooled at a fast rate (ΔT 500–1000 °C/h). Closer to the melt pocket margin, elongate skeletal olivine shapes progress to hopper and equant euhedral shapes, reflecting an increase in nuclei in the melt at the initiation of crystallization and growth at low degrees of supercooling. During crystallization the oxygen fugacity is buffered at <FMQ − 2. The results of this study place some limits on models of melt pocket formation.

1. The melting process is just as important, if not more so, than cooling in determining the final texture of the melt pocket, as this processes controls elimination or preservation of nuclei at the onset of cooling and crystallization.
2. The formation of melt pockets having high liquidus temperatures (>1500 °C) involves incomplete melting of crystalline precursor material.
3. Melt pockets with relatively low liquidus temperatures (~1200–1400 °C) most likely crystallize from superheated melts.
4. The local hot spots, generated in the target rock during shock, reach temperatures of at least 1510–1520 °C for the ALH 77005 melt pocket investigated in this study; however, temperatures could have been higher but only for a short period of time.
5. Melt pocket forming events are of short duration (10s of minutes).
6. The oxygen fugacity of shock melts are set by the redox state (Fe^{3+}/Fe^{2+} ratio) of the host rock material undergoing melting, and is not externally imposed.
7. Trapped gases in melt pockets require that precursor material is connected to the Martian atmosphere, yet melt pockets consist of material that is locally melted, not injected.

ACKNOWLEDGMENTS

This work has been funded by the Natural Sciences and Engineering Research Council of Canada (NSERC), the Canadian Space Agency and the Alberta Ingenuity Fund through grants awarded to ELW, and NSERC Discovery Grant 261740-03 to CDKH. The authors gratefully acknowledge the Antarctic Meteorite Working Group for loan of the ALH 77005, 122 thin section. Thanks to Sergei Matveev (UA) and Douglas Hall (UNB) for EM assistance and George Braybrook for FE-SEM assistance. Reviews by Gary Lofgren, David Draper, Takashi Mikouchi and the associate editor, David Mittlefehldt, improved the quality of the manuscript.

REFERENCES

Artemieva N. and Ivanov B. (2004) Launch of Martian meteorites in oblique impacts. *Icarus* **171**, 84–101.

Beck P., Gillet P., Gautron L., Daniel I. and El Goresy A. (2004) A new natural high-pressure (Na,Ca)-hexaluminosilicate [$(Ca_{x}Na_{1-x})Al_{3+x}Si_{3-x}O_{11}$] in shocked Martian meteorites. *Earth Planet. Sci. Lett.* **219**, 1–12.

Beck P., Ferroir T. and Gillet P. (2007) Shock-induced compaction, melting, and entrapment of atmospheric gases in Martian meteorites. *Geophys. Res. Lett.* **34**, L01203. doi:10.1029/2006GL028141.

Becker R. H. and Pepin R. O. (1984) The case for a Martian origin of the shergottites: nitrogen and noble gases in EETA 79001. *Earth Planet. Sci. Lett.* **69**, 225–242.

Bianco A. S. and Taylor L. A. (1977) Applications of dynamic crystallization studies: lunar olivine normative basalts. *Proc., Lunar Sci. Conf.* **8**, 1593–1610.

Bland P. A. and Artemieva N. A. (2003) Efficient disruption of small asteroids by Earth's atmosphere. *Nature* **424**, 288–291.

Bogard D. D. and Garrison D. H. (1999) ^{39}Ar–^{40}Ar "ages" and trapped argon in Martian shergottites, Chassigny and Allan Hills 84001. *Meteor. Planet. Sci.* **34**, 451–473.

Bogard D. D. and Johnson P. (1983) Martian gases in an Antarctic meteorite? *Science* **221**, 651–654.

Bogard D. D., Hörz F. and Johnson P. (1986) Shock-implanted noble gases: an experimental study with implications for the

origin of Martian gases in shergottite meteorites. *J. Geophys. Res.* **91**(B13), E99–E114.

Bogard D. D., Hörz F. and Johnson P. H. (1989) Shock-implanted noble gases: an experimental study with implication for the origin of Martian gases in shergottite meteorites. *J. Geophys. Res.* **91**(B13), E99–E114.

Carmichael I. S. E. (1967) The iron-titanium oxides of salic volcanic rocks and their associated ferromagnesian silicates. *Contrib. Miner. Petrol.* **14**, 36–64.

Carr R. H., Grady M. M., Wright I. P. and Pillinger C. T. (1985) Martian atmospheric carbon dioxide and weathering products in SNC meteorites. *Nature* **314**, 248–250.

Ceplecha Z., Spurný P., Borovička J. and Keclíková J. (1993) Atmospheric fragmentation of meteoroids. *Astron. Astrophys.* **279**, 615–626.

Davis B. T. C. and England J. L. (1964) The melting of forsterite up to 50 kilobars. *J. Geophys. Res.* **69**, 1113–1116.

DeHart J. M. and Lofgren G. E. (1996) Experimental studies of group A1 chondrules. *Geochim. Cosmochim. Acta* **60**, 2233–2242.

Donaldson C. H. (1976) An experimental investigation of olivine morphology. *Contrib. Mineral. Petrol.* **57**, 187–213.

Dowty E. (1980) Crystal growth and nucleation theory and the numerical simulation of igneous crystallization. In *Physics of Magmatic Processes* (ed. R. B. Hargrave). Princeton University Press, Princeton, pp. 419–485.

Eugster O., Busemann H., Lorenzetti S. and Terribilini D. (2002) Ejection ages from ^{81}Kr–^{83}Kr dating and pre-atmospheric sizes of Martian meteorites. *Meteor. Planet. Sci.* **37**, 1345–1360.

French B. M. (1998) *Traces of Catastrophe: A Handbook of Shock-Metamorphic Effects in Terrestrial Meteorite Impact Structures*. Lunar and Planetary Institute, Houston, 120 pp. LPI Contribution No. 954.

Gago-Duport L., de la Rosa N. and Garcia-Ruiz J. M. (1995) Nucleation and clustering: a microscopic study of the aggregation behavior in metastable solutions. *J. Non-Cryst. Solids* **192**, 503–508.

Gooding J. L. and Muenow D. W. (1986) Martian volatiles in shergottite EETA 79001: new evidence from oxidized sulfur and sulfur-rich aluminosilicates. *Geochim. Cosmochim. Acta* **50**, 1049–1059.

Goodrich C. A., Herd C. D. K. and Taylor L. A. (2003) Spinels and oxygen fugacity in olivine-phyric and lherzolitic shergottites. *Meteor. Planet. Sci.* **38**, 1773–1792.

Grove T. L. and Beaty D. W. (1980) Classification, experimental petrology, and possible volcanic histories of the Apollo 11 high-K basalts. *Proc., Lunar Sci. Conf.* **11**, 149–177.

Heider N. and Kenkmann T. (2003) Numerical simulation of temperature effects at fissures due to shock loading. *Meteor. Planet. Sci.* **38**, 1451–1460.

Herd C. D. K. (2006) An occurrence of jarosite in MIL 03346: Implications for conditions of martian aqueous alteration. *Meteor. Planet. Sci.* **41**, A74, abstr.

Herd C. D. K., Papike J. J. and Brearley A. J. (2001) Oxygen fugacity of Martian basalts from electron microprobe oxygen and TEM-EELS analyses of Fe–Ti oxides. *Am. Miner.* **86**, 1015–1024.

Karner J. M., Sutton S. R., Papike J. J., Shearer C. K., Jones J. H. and Newville M. (2006) Application of a new vanadium valence oxybarometer to basaltic glasses from the Earth, Moon, and Mars. *Am. Miner.* **91**, 270–277.

Keith H. D. and Padden, Jr., F. J. (1963) A phenomenological theory of spherulite crystallization. *J. Appl. Phys.* **34**, 2409–2421.

Kirkpatrick R. J. (1975) Crystal growth from the melt. *Am. Miner.* **60**, 798–814.

Langenhorst F. (2002) Shock metamorphism of some minerals: Basic introduction and microstructural observations. *Bull. Czech Geol. Surv.* **77**, 265–282.

Lofgren G. E. (1977) Dynamic crystallization experiments bearing on the origin of textures in impact generated liquids. *Proc., Lunar Sci. Conf.* **8**, 2079–2095.

Lofgren G. E. (1980) Experimental studies on the dynamic crystallization of silicate melts. In *Physics of Magmatic Processes* (ed. R. B. Hargrave). Princeton University Press, Princeton, pp. 487–551.

Lofgren G. E. (1983) Effect of heterogeneous nucleation on basaltic textures: a dynamic crystallization study. *J. Petrol.* **24**, 225–229.

Lofgren G. E. (1989) Dynamic crystallization of chondrule melts of porphyritic olivine composition: textures experimental and natural. *Geochim. Cosmochim. Acta* **53**, 461–470.

Lofgren G. and Russell W. J. (1986) Dynamic crystallization of chondrule melts of porphyritic and radial pyroxene composition. *Geochim. Cosmochim. Acta* **50**, 1715–1726.

Lofgren G., Donaldson C. H., Williams R. J., Mullins O., Jr. and Usselman M. (1974). Experimentally reproduced textures and minerals chemistry of Apollo 15 quartz normative basalts. *Proc., Lunar Sci. Conf.* **5**, 549–567.

Lofgren G. E., Grove T. L., Brown R. W. and Smith D. P. (1979) Comparison of dynamic crystallization techniques on Apollo 15 quartz normative basalts. *Proc., Lunar Sci. Conf.* **10**, 423–438.

Marti K., Kim J. S., Thakur A. N., McCoy T. J. and Keil K. (1995) Signatures of the Martian atmosphere in glass of the Zagami meteorite. *Science* **267**, 1983–1984.

McKay G., Le L., Schwandt C., Mikouchi T., Koizumi E. and Jones J. (2004) Yamato 980459: the most primitive shergottite? *Lunar Planet. Sci. XXXV*. Lunar Planet. Inst., Houston. #2154 (abstr.).

McSween Jr., H. Y. and Jarosewich E. (1983) Petrogenesis of the Elephant Moraine A79001 meteorite: multiple magma pulses on the shergottite parent body. *Geochim. Cosmochim. Acta* **47**, 1501–1513.

McSween Jr., H. Y. and Keil K. (2000) Mixing relationships in the Martian regolith and the composition of globally homogeneous dust. *Geochim. Cosmochim. Acta* **64**, 2155–2166.

Meyer C. (2007) Mars meteorite compendium. http://curator.jsc.nasa.gov/antmet/mmc/index.cfm.

Nyquist L., Wiesman H., Shih C.-Y. and Bansal B. (1986) Sr isotopic systematics of EETA 79001 glass. *Lunar. Planet. Sci. XVII.* Lunar Planet. Inst., Houston. pp. 624–625 (abstr.).

Pohl J., Stöffler D., Gall H. and Ernston K. (1977) The Ries impact crater. In *Impact and Explosion Cratering* (eds. D. H. Roddy, R. O. Pepin and R. B. Merill). Pergamon Press, New York, pp. 343–404.

Rao M. N., Borg L. E., McKay D. S. and Wentworth S. J. (1999) Martian soil component in impact glasses in a Martian meteorite. *Geophys. Res. Lett.* **26**, 3265–3268.

Owen T., Biemann K., Rushneck D. R., Howarth D. W. and Lafleur A. L. (1977) The composition of the atmosphere at the surface of Mars. *J. Geophys. Res.* **82**, 4635–4639.

Schaal R. B. and Hörz F. (1977) Shock metamorphism of lunar and terrestrial basalts. *Proc. Lunar Sci. Conf.* **8**, 1697–1729.

Sharp T. G. and DeCarli P. G. (2006) Shock effects in meteorites. In *Meteorites and the Early Solar System II* (eds. H. Y. McSween Jr. and D. S. Lauretta). University of Arizona Press, Tucson, pp. 653–677.

Stewart S. T., Seifter A., Kennedy G. B., Furlanetto M. R. and Obst A. W. (2007) Measurements of emission temperatures from shocked basalt: hot spots in meteorites. *Lunar Planet. Sci. XXXVIII*. Lunar Planet. Inst., Houston. #2413 (abstr.).

Stöffler D. and Ostertag R. (1983) The Ries impact crater. *Fortschr. Mineral.* **61**, 71–116.

Treiman A. H. (2005) The nakhlite meteorites: Augite-rich igneous rocks from Mars. *Chem. Der Erde-Geochem.* **65**, 203–270.

Treiman A. H., Barrett R. A. and Gooding J. L. (1993) Preterrestrial aqueous alteration of the lafayette (SNC) meteorite. *Meteoritics* **28**, 86–97.

Treiman A. H., McKay G. A., Bogard D. D., Mittlefehldt D. W., Wang M.-S., Keller L., Lipschultz M. E., Lindstrom M. M. and Garrison D. (1994) Comparison of the LEW88516 and ALHA77005 Martian meteorites: similar but distinct. *Meteoritics* **29**, 581–592.

Tsuchiyama A., Nagahara H. and Kushiro L. (1980) Experimental reproduction of textures of chondrules. *Earth Planet. Sci. Lett.* **48**, 155–165.

Turnbull D. (1950) Kinetics of heterogeneous nucleation. *J. Chem. Phys.* **18**, 198–203.

Uhlmann D. R. and Chalmers B. (1965). *Nucleation Ind. Eng. Chem.* **57**, 19–31.

Usselman T .M. and Lofgren G. E. (1976) The phase relations, textures, and mineral chemistries of high titanium mare basalts as a function of oxygen fugacity and cooling rate. *Proc., Lunar Sci. Conf.* **7**, 1345–1363.

Vicenzi E. P., Fries M., Fahey A., Rost D., Greenwood J. P. and Steele A. (2007) Detailed elemental, mineralogical, and isotopic examination of jarosite in Martian meteorite MIL 03346. *Lunar Planet. Sci. XXXVIII*, Lunar Planet. Inst., Houston. #2335 (abstr.).

Walton E. L. and Herd C. D. K. (2007) Localized shock melting in lherzolitic shergottite Northwest Africa 1950: comparison with Allan Hills 77005. *Meteor. Planet. Sci.* **42**, 1–18.

Walton E. L. and Spray J. G. (2003) Mineralogy, microtexture, and composition of shock-induced melt pockets in the Los Angeles basaltic shergottite. *Meteor. Planet. Sci.* **38**, 1865–1875.

Walton E., Shaw C., Cogswell S. and Spray J. (2006) Crystallization rates of shock melts in three Martian basalts: experimental simulation with implications for meteoroid launch diameters. *Geochim. Cosmochim. Acta* **70**, 1059–1075.

Walton E. L., Kelley S. P. and Spray J. G. (2007) Shock implantation of Martian atmospheric argon in four basaltic shergottites: a laser probe $^{40}Ar/^{39}Ar$ investigation. *Geochim. Cosmochim. Acta* **71**, 497–520.

Wiens R. C. (1988) On the siting of gases shock-emplaced from internal cavities in basalt. *Geochim. Cosmochim. Acta* **52**, 2775–2785.

Wiens R. C. and Pepin R. O. (1988) Laboratory shock emplacement of noble gases nitrogen, and carbon dioxide into basalt, and implications for trapped gas in shergottite EETA79001. *Geochim. Cosmochim. Acta* **52**, 295–307.

Wiens R. C., Becker R. H. and Pepin R. O. (1984) The case for a Martian origin of the shergottites: II. Trapped and indigenous gas components in EETA 79001 glass. *Earth Planet. Sci.* **7**, 149–158.

Wones D. R. and Gilbert M. C. (1969) Fayalite–Magnetite–Quartz assemblage between 600 and 800 °C. *Am. J. Sci.* **267A**, 480–488.

Wooden J., Shih C.-Y., Nyquist L., Bansal B., Wiesmann H. and McKay G. (1982) Rb–Sr and Sm–Nd isotopic constraints on the origin of EETA 79001: a second Antarctic shergottite. *Lunar Planet. Sci. XIII.* Lunar Planet. Inst., Houston. pp. 879–880 (abstr.).

Yen A. S., Kim S. S., Hecht M. H., Frant M. S. and Murray B. (2000) Evidence that the reactivity of the martian soil is due to superoxide ions. *Science* **289**, 1909–1912.

Yinnon H., Roshko A. and Uhlmann D. R. (1980) On the barrier to crystal nucleation in lunar glasses. *Proc. Lunar Sci. Conf.* **11**, 197–211.

Zent A. P. and McKay C. P. (1994) The chemical-reactivity of the Martian soil and implications for future missions. *Icarus* **108**, 146–157.

Associate editor: David W. Mittlefehldt